The Pennsylvania State University

The Graduate School

College of Earth and Mineral Sciences

MICROWAVE SCATTERING FROM MELTING ICE CRYSTALS

A Thesis in

Meteorology

by

Kristina M. Baker

Submitted in Partial Fulfillment
of the Requirements
for the Degree of

Master of Science

December 2009

The thesis of Kristina M. Baker was reviewed and approved* by the following:

Johannes Verlinde
Associate Professor of Meteorology
Thesis Adviser
Head of the Graduate Department

Kultegin Aydin
Professor of Electrical Engineering

Eugene E. Clothiaux
Associate Professor of Meteorology

William H. Brune
Professor of Meteorology
Head of the Department of Meteorology

*Signatures are on file in the Graduate School.

ABSTRACT

Simple configurations of aligned spheres were created to simulate cross-shaped and column-shaped ice crystals to examine differential reflectivity during melting using a computational model for calculating scattering properties of multi-sphere configurations. The model, developed by Daniel W. Mackowski, is based upon an analytical solution to Maxwell's wave equation for non-overlapping spheres. The goal was to recreate anomalous differential reflectivity, Z_{DR}, readings, known as the radar bright band, that are noted in field measurements. Microwave scattering from single, horizontally oriented crystals was first examined. Subsequent simulations introduced rotation and canting of the crystal proxy over 500 realizations as it falls through the melting layer. The results of these simulations are shown and discussed. These simple experiments support the presence of the large maximum in Z_{DR} observed in the radar bright band.

TABLE OF CONTENTS

LIST OF FIGURES

LIST OF TABLES

Chapter 1

Introduction

The melting layer of precipitation can be described as the horizontal section of the atmosphere below the zero degree isotherm where ice crystals and aggregates melt into raindrops. This melting region coincides with a phenomenon known as the radar bright band, an area of enhanced radar reflectivity. The study of the melting layer is well-documented in observation and experiment (Mitra et al., 1990; Fabry and Zawadzki, 1995; Ryzhkov and Zrnic, 1998); numerical modeling attempts are also published (Klaasen, 1988; Drummond et al., 1996; Russchenberg and Lighthard, 1996; Meneghini and Liao, 1996; D'Amico et al., 1998; Szyrmer and Zawadzki, 1999; Skaropoulos and Russchenberg, 2003). An increasing use of microwave frequencies for satellite communication and space-based cloud and precipitation remote sensing platforms warrants a deeper understanding of the influence of the melting layer on absorption and scattering of electromagnetic radiation.

In order to develop a model capable of accurately recreating the effects of the melting layer on electromagnetic radiation, we first must consider the detailed wind tunnel study of melting snow flakes made by Mitra et al. (1990). Melting initiates some distance after the hydrometeors fall past the zero degree isotherm, the exact distance determined by the relative humidity of the ambient air and its impact on the heat transfer characteristics of the system. Once melting begins, small water droplets, with a diameter on the order of tens of microns, form on the periphery of the ice crystal structure. As melting proceeds, the meltwater flows to linkages of ice branches where the water accumulates. The small branches in the flake interior melt, while the flake density increases as it changes from one "with many small openings to one with a few large openings." The ice frame collapses suddenly and afterwards the hydrometeor pulls itself together into a drop shape.

The laboratory work discussed by Mitra et al. (1990) revealed that the hydrometeor is a complicated, inhomogeneous mixture of ice, water and air as it falls

through the melting layer. Previously, computational limitations required the assumption that the hydrometeor be represented as a homogeneous mixture, the equivalent medium dielectric constant approximated by one of the various mixing formulas, such as the Maxwell-Garnett (i.e. Bohren and Battan, 1980; Klaasen, 1988; Drummond et al., 1996; Russchenberg and Lighthart, 1996; Meneghini and Liao, 1996; D'Amico et al., 1998; Skaropoulos and Russchenberg, 2003) or the multi-phase mixing formula (Ulaby et al., 1986). The exact manner of use of the Maxwell-Garnett approximation itself is not obvious, as different researchers, relying on different topologies of the melting hydrometeors, make different assumptions regarding the calculation of the effective permittivity. For example, Russchenberg and Lighthart (1996) assume that the effective permittivity is the weighted average of the Maxwell-Garnett mixing formula for two different topologies, the first assuming snow inclusions in a water matrix and the second assuming water inclusions in a snow matrix, while Fabry and Szyrmer (1999) tested six different formulations for their modeling study. In consideration of the array of approaches assumed, it is no surprise that Szyrmer and Zawadzki (1999) acknowledge that the largest source of uncertainty when comparing predicted scattering properties to the actual radar data is the assumption made with regards to the structure and melting process of the snow at a microphysical scale.

In this thesis, we explore an alternative way to represent melting hydrometeors in a scattering code that radically deviates from the equivalent medium approach used in previous studies. In this initial explorative study, we seek to take advantage of the greater computational power and recent advances in modeling electromagnetic scattering from complicated shaped particles (Mackowski, 1999; Xu, 1995), where the complex hydrometeor is represented as a cluster of spheres. This approach is motivated by a hypothesis presented by Verlinde et al. (2002), hereafter V02, based on high quality polarimetric radar measurements of the melting layer. V02's hypothesis is presented in Chapter 2; Chapter 3 explains the scattering model used; the results of our simulations are discussed in Chapter 4; and a general discussion follows with conclusions in Chapter 5.

Chapter 2

Background

Recent observations of the melting layer with polarimetric radars provide a new look at melting layer processes and an opportunity to implement stronger constraints on modeling activities. V02 presented radar data obtained during continuous, widespread rain in the Netherlands. These data were collected using the Technical University of Delft Transportable Atmospheric Radar (TARA), which allowed for polarimetric measurements of unprecedented vertical resolution through precipitating cloud layers. A major focus of the presentation, which is carried on to this thesis, is the calculation of differential reflectivity from the radar data. Differential reflectivity, Z_{DR}, is defined as the ratio of returned power from horizontal to vertical polarized pulses (Seliga and Bringi, 1976):

$$Z_{DR} = 10 \log \frac{Z_{HH}}{Z_{VV}}.$$

The focus on Z_{DR} in bright band studies is not unprecedented; Ryzhkov and Zrnic (1998) found that the Z_{DR} maximum is an effective tool for isolating the bright band and locating the snow-rain boundary. Z_{DR} can also be used to assess types and sizes of hydrometeors as summarized by Straka et al. (2000).

V02 utilized the capabilities of TARA to calculate another unique quantity, the spectral differential reflectivity, or sZ_{DR}. Spectral differential reflectivity is defined as the ratio of the horizontal and vertical reflectivities of scatters in the radar resolution volume moving with similar radial speeds within a small velocity increment. Combining sZ_{DR} values from increments across the entire Nyquist velocity range produces a velocity – differential reflectivity spectrum. By combining spectra from all range gates one creates a spectrograph, a contour map of sZ_{DR} as a function of velocity and height (Figure 1). V02 averaged spectrographs from a one minute period to produce a spectrograph of mean sZ_{DR}. They also defined a spectrograph of the time variability of sZ_{DR}, or σ^{t}_{sZDR}, as the standard deviation in time of sZ_{DR} values for each velocity bin.

The spectrographs generated from the TARA data presented a unique and detailed view of the melting layer not seen before. In the discussion of the data, V02 presented a comprehensive interpretation of the spectrographs of reflectivity (Z_{HH}), sZ_{DR}, and σ^{t}_{sZDR}, the details of which we summarize below.

Figure 1 presents spectrographs of spectral reflectivity Z_{HH}, spectral differential reflectivity sZ_{DR} and the time variability of spectral reflectivity σ^{t}_{sZDR} for the case observed on 19 September 2001 at the Royal Netherlands Meteorological Institute research site at Cabauw in the Netherlands. A thick precipitating cloud layer, extending from 1.7 km to 9.0 km in height, produced steady rain for hours during this event. A nearby radiosonde sounding indicated that the freezing level at the time of these measurements was located at 1850 m, just above cloud base, but the radar measurements and other radiosondes indicated that the freezing level height fluctuated within a 300 m range (1.8 km to 2.1 km).

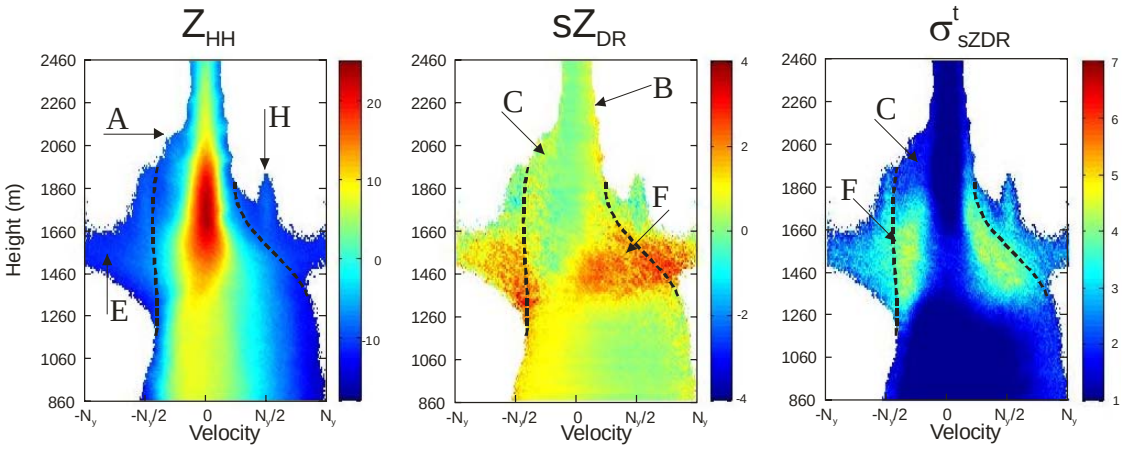

Figure 1. Spectrographs of spectral reflectivity Z_{HH}, spectral differential reflectivity sZ_{DR} and the time variability of spectral reflectivity σ^{t}_{sZDR}. Individual spectra were aligned such that the Z_{HH} spectrum peaks are located at the zero velocity bins at each height. In this case, the radar antenna was kept at a constant azimuth, with elevation angle 45 degrees. Please note that negative velocity is toward the radar (Adapted from V02).

V02 identified several distinct features in the spectrographs:

A) The first indication of melting is noted by the formation of faster falling aggregates producing a shift in the co-polar Z_{HH} signal to the left, coinciding with an increase in co-polar reflectivity in the core of the spectrum and an initial detection of cross-polar HV signal (not shown).

B) Above the melting layer, oriented, pristine ice crystals produce high spectral sZ_{DR} values of approximately 1 db.

C) During aggregation, the sZ_{DR} values show uniformity around ~1 db, indicating that these aggregates in the upper part of the melting layer fall with a preferred oblate orientation.

E+H) The shoulders on the spectrographs are processing artifacts. During the final stage of melting, the ice structure collapses, resulting in a large change in the shape and dielectric properties of the hydrometeors within the FFT data collection period producing spectral leakage.

F) Just before the collapse of the ice structure, the hydrometeors remain mostly oblate and have the highest bulk densities and dielectric constants. The net result is a mean sZ_{DR} value of around +2 db, although these values fluctuate wildly (± 6 db). A possible explanation is the erratic linear and curved motions of the hydrometeors coupled with the spinning and helical swinging motions observed by Mitra et al. (1990).

Most of these features can be reproduced using a bulk parameterization for the material properties of the mixed phase hydrometeors, with each hydrometeor assumed to consist of a homogeneous mixture of air, liquid and ice, the equivalent medium dielectric constant of which may be calculated from one of the various mixing formulas (i.e. Maxwell-Garnett theory (Bohren and Battan, 1980) or the multi-phase mixing formula (Ulaby et al. 1986). Indeed, a modeling study by Skaropoulos et al. (2003) was able to produce most of these features. However, V02 argued that some of the finer details, such as the very large σ^{t}_{sZDR} values in the lower parts of the melting layer, are

inconsistent with the homogeneous mixture assumption, and relied on the laboratory work of Mitra et al. (1990) to suggest an alternative way to view scattering from a melting aggregate.

When millimeter to centimeter size aggregates melt, we can expect that the initial melt drops forming at the tips of ice crystals protruding from the aggregate (Mitra et al., 1990) are generally well separated. The ice structure of the aggregate acts as a skeleton for the hydrometeor during melting, so that individual melt drops only slowly migrate towards the aggregate core. At the same time the larger structure of the aggregate determines its fall characteristics. As melting proceeds, the effective dielectric constant of the aggregate must increase, hence the reflectivity will increase. V02 argued that this increase may largely be influenced by the growing liquid melt drops, and not by the ice structure. The liquid droplets have a significantly different dielectric constant from the solid ice structure and could dominate scattering by acting initially as non-interacting coherent scatterers. As a consequence, they argued that the homogeneous medium model may not be the appropriate model to use for melting aggregates, but that a model that accounts for the number and location of the liquid droplets in the ice structure may be necessary. Such models exist. For example, Mackowski (1994) developed a cluster-of-spheres code that incorporates much of the hypothesized scattering physics.

The TARA data present an opportunity to test new hypotheses of the details of the melting process in the bright band and its effect on radar signatures. The hypothesis developed by V02 and further investigated by Baker and Verlinde (2004) states that these initial, individual melt drops and their interaction with each other during the course of melting dominate the scattering properties of the low-density aggregates. The merging of two droplets could be a source for the anomalous scattering phenomenon due to interaction of the electromagnetic field induced in each of the droplets by the incident radar beam. The effect might only be seen for limited time periods during the melting process when droplet pairs become close enough to interact.

Initially, when the melt drops are at the periphery of the aggregate and remain well-separated, the contribution to the aggregate sZ_{DR} by the liquid is that of the individual drops (i.e. zero db), and the contribution of the ice structure (shape) dominates. As melting progresses, the proportion of water in the aggregate increases and the melt drops grow while simultaneously migrating toward the center of the aggregate, perhaps contributing to a flattening of the sZ_{DR} slope in the fall velocity range pertinent to these aggregates (see Figure 5 in V02). At this point the periphery of the aggregate is mostly dry, with the inner ice structure surrounded by the converging melt water. The smaller ice branches in the structure melt first, and there is a period of melting at this point when the overall ice structure size and oblate shape remain mostly constant while the nature of the aggregate changes from an ice structure with many small openings to an ice structure with a few large openings. The resulting hydrometeor is a fragment of the initial ice skeleton completely surrounded by water in a drop shape, corresponding to a sudden decrease in Z_{DR} appropriate for a liquid drop.

This area of research has become of renewed interest with the acquisition of X-band (3.1 cm), Ka-band (0.86 cm), and W-band (0.3 cm) wavelength polarimetric radars by the Atmospheric Radiation Measurement (ARM) Program. The present goal is to investigate the validity of V02's hypothesis using simplified proxies of melting ice crystals, composed of lines of spheres and described in Chapter 3. When Baker and Verlinde (2004) modeled a melting ice aggregate by calculating the scattering effects from only the liquid water drops and ignoring the ice lattice entirely, the results of this initial melting aggregate simulation showed some promise and produced variation in Z_{DR}. Subsequent discussions of the validity of the cluster of liquid water spheres method for simulating melting aggregates centered on the possible adverse impact of removing the ice lattice; two sphere melting simulations had shown that there is a significant interaction between an ice sphere and a water sphere (see Chapter 4). Rather than attempting to develop a model of the full melting process for aggregates that includes both the water and ice, we decided to do an exploratory study of the potential impacts of the melting process on radar backscattering for simplified ice structures.

The use of simplified crystals allows the examination of the central statement of V02's hypothesis, that in fact a large variability in Z_{DR} is produced by melting the tips of crystals and bringing the melt drops into the center. The simplified model allows the examination of the effect of type and size of aggregate, along with the impact of water-water, ice-ice, and water-ice interactions. These simple modeling experiments can be used to eventually develop a more comprehensive melting model for aggregates which functions similarly to the simpler models by forming a shape using a number spheres of differing refractive indices. These aggregates would be melted systematically in a process that more accurately models the behavior of aggregates observed by Mitra et al. (1990) and described above.

Chapter 3

Cluster of Spheres Computational Model

Baker and Verlinde (2004) evaluated several scattering algorithms to find the most appropriate and accurate computational solution. Discrete dipole approximation (DDA), developed by Draine and Flatau (1994), replaces an object with an array of discrete dipoles, allowing the scattering calculations to be solved exactly. Despite the usefulness of the DDA method in many applications, the code is most appropriately used for objects with a refractive index near unity; its accuracy decreases as $|m|$ increases (Draine and Flatau, 1994). This method may have been useful for modeling the ice portion of the aggregate during melting, but it becomes sufficiently inaccurate for water spheres that additional methods were explored.

Mackowski (1994) developed a formal solution of the radiative scattering for an arbitrary configuration of neighboring spheres based upon an analytical solution to Maxwell's wave equation for non-overlapping spheres. Baker and Verlinde (2004) utilized the Mackowski multi-sphere code (available on the web at http://atol.ucsd.edu/scatlib/scatterlib.htm) to calculate the scattering properties of the liquid water droplets melting model. For calculating the differential reflectivity, Z_{DR}, and other polarimetric scattering properties of the column and cross cluster of spheres models, we found that Mackowski's code was the most appropriate and accurate for our purposes.

The user can manipulate the angle of the incident field to illuminate the cluster of spheres from a number of different angles after specifying a field of spheres. All elements of the amplitude scattering matrix (S_1, S_2, S_3, and S_4) (Bohren and Huffman, 1983) are calculated given an array of spheres with their locations, sizes, and refractive indices, along with the details of the incident electromagnetic wave. These elements can be used to calculate several scattering properties, including Z_{DR}.

Rotation and canting of sphere configurations are accomplished through an Euler rotation of the cluster of spheres from the original right-handed frame of reference (*x*, *y*, *z*) to the new set of axes (*x*′, *y*′, *z*′):

1. The cluster is rotated **α** about the *z*-axis;
2. The new frame is rotated **β** about the ***new*** *y*-axis;

Figure 2 illustrates the coordinate system and rotation process for a line of spheres. In this case, we adopted the Mackowski frame of reference, in which the incident field propagates in the *z*′ direction and the particles lie in the *x*-*z* plane. Physically, this corresponds to air-based radar sending a signal horizontal to the horizon into the mixed phase cloud. Canting of the crystals is simulated by varying α between -10° and 10° using a random normal distribution; varying β between 0° and 90° using a random uniform distribution corresponds to the random horizontal orientation of the crystals as they fall.

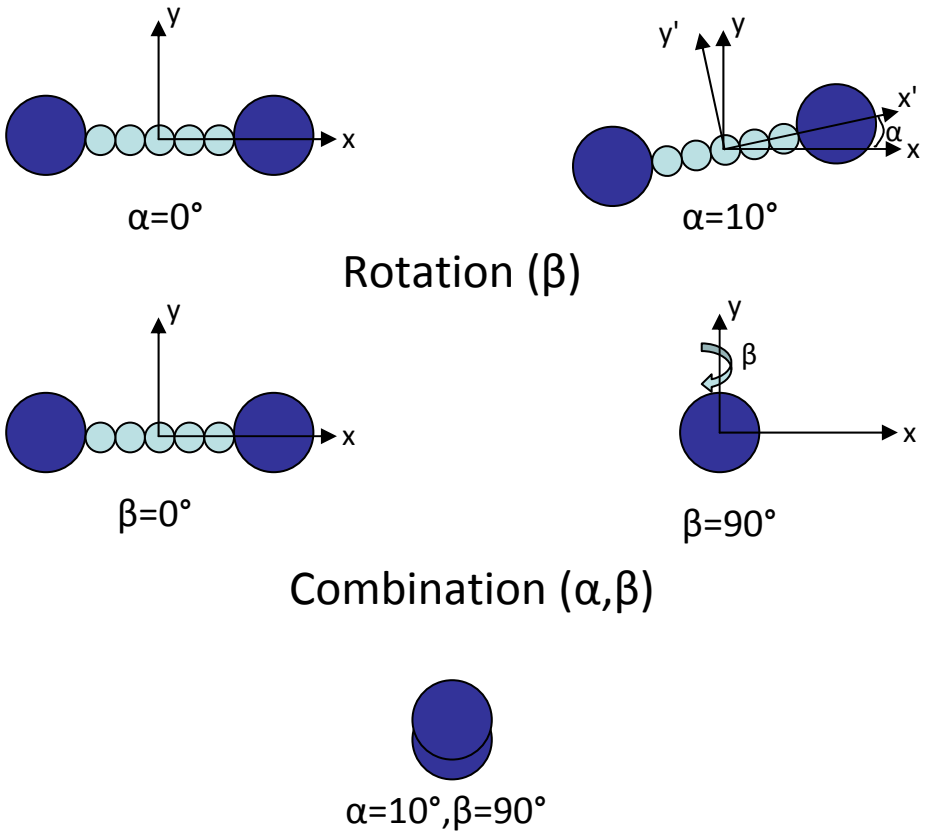

Figure 2. Illustration of rotation and canting of a sphere configuration. In this case, the *z*-axis points from the reader into the paper.

Two Sphere Experiment

In order to understand the effect of sphere size and composition on the scattering properties of interacting spheres, we conducted several simple experiments examining two spheres located along an x-axis. Z_{DR} is calculated as the spheres are brought closer together until only 1 μm separates them; at no point in the experiment do the spheres overlap. Results were generated for spheres of 10 μm, 20 μm, 50 μm, and 100 μm radii at four radar wavelengths: 9.09 cm, 3.1 cm, 0.86 cm, and 0.30 cm. Three scenarios are explored: two water spheres, two ice spheres, and one ice sphere and one water sphere. Results are presented in Chapter 4 and provide significant insight into the relative importance of ice-ice, ice-water, and water-water interactions, along with the overwhelming impact the distance between the spheres has on Z_{DR}. The results of the two sphere simulations are paramount to the interpretation of the column and cross simulations discussed next.

The Column and Cross Model

In order to eliminate the complexity produced by a model of a melting ice aggregate, we explored simple columnar and cross-shaped ice crystals, which can provide valuable information for interpreting the polarimetric scattering signature of falling, melting hydrometeors. In the simulations, lines of spheres make up the arms of the crystal, and the radius of the spheres is derived from the relationship of crystal arm length (*L*) to width (*d*) as listed in Auer and Veal (1970) for simple column crystals (N1e) and in Pruppacher and Klett (1983) for a cross-shaped crystal (P1d, page 51), where *d* and *L* are in cm:

$$\text{N1e}: \; d = 3.527 \times 10^{-2} L^{0.437}$$

$$\text{P1d}: \; d = 9.96 \times 10^{-3} L^{0.415}$$

Both column and cross-shaped crystals were generated targeting an overall length of approximately 200 μm, 750 μm, 1500 μm, and 3000 μm. These lengths were entered into the equations above to determine a corresponding thickness, d. Whole spheres of

diameter, d, were aligned in a column or a cross shape consecutively until the length was no greater than 200 μm, 750 μm, 1500 μm, or 3000 μm. Table 1 lists the arm thickness for all lengths for the column and cross shaped crystals.

Table 1. Arm thickness and total mass for column-shaped and cross-shaped crystals for differing overall crystal length, *L*.

Approximate crystal length (*L*) in μm	Column thickness *d* (μm)	Total Column crystal mass (mg)	Cross arm thickness *d* (μm)	Total Cross crystal mass (mg)
200	63.8	0.117	19.6	0.0774
750	113.7	0.869	34.0	0.499
1500	153.9	2.05	45.3	1.28
3000	208.4	6.25	60.4	3.40

Figures 3 and 4 illustrate the melting process simulation. Melting progresses in a stepwise fashion with the outermost spheres becoming water. The size of the spheres is adjusted based on the change in density from ice to water. In the next step of melting, the next outermost spheres change from ice to water and join the initial water spheres. The size of this larger water sphere is calculated from the total mass of the two spheres and the density of water. The process continues until there is simply one large water sphere at the center of the crystal. Note that in Figures 3 and 4, the radar signal propagates in the *z*-direction.

The first set of analyses focused on one simple column and one simple cross without the effects of canting or rotation, with the cluster of spheres lying in the *x*-*z* plane. Subsequently, five hundred simulations were generated per melt step, allowing for both canting and rotation of the crystals. Figure 2 illustrates the introduction of rotation and canting for a column crystal; Figure 5 shows the equivalent geometry for a cross crystal.

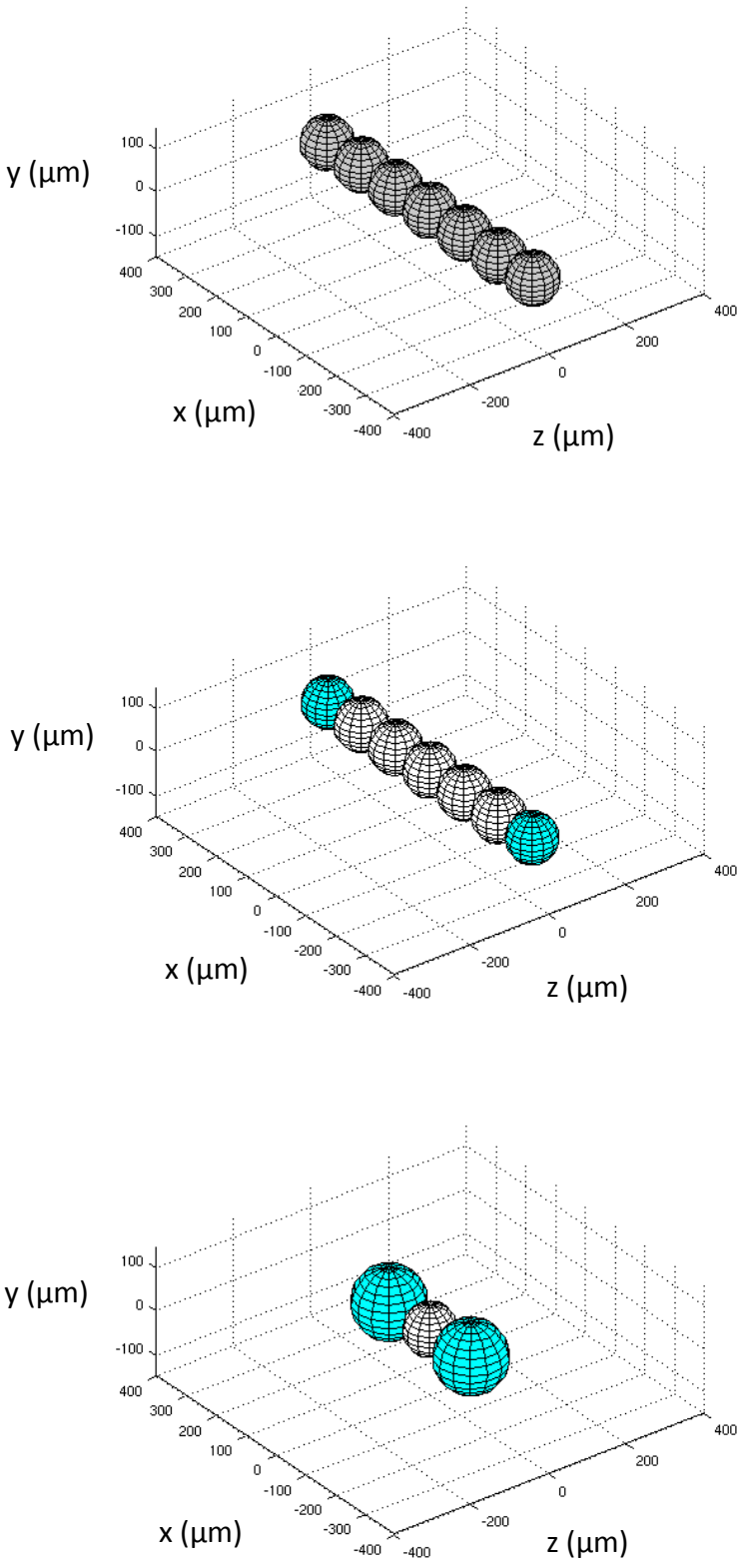

Figure 3. Diagram of the process of melting a column crystal (L=750 μm).

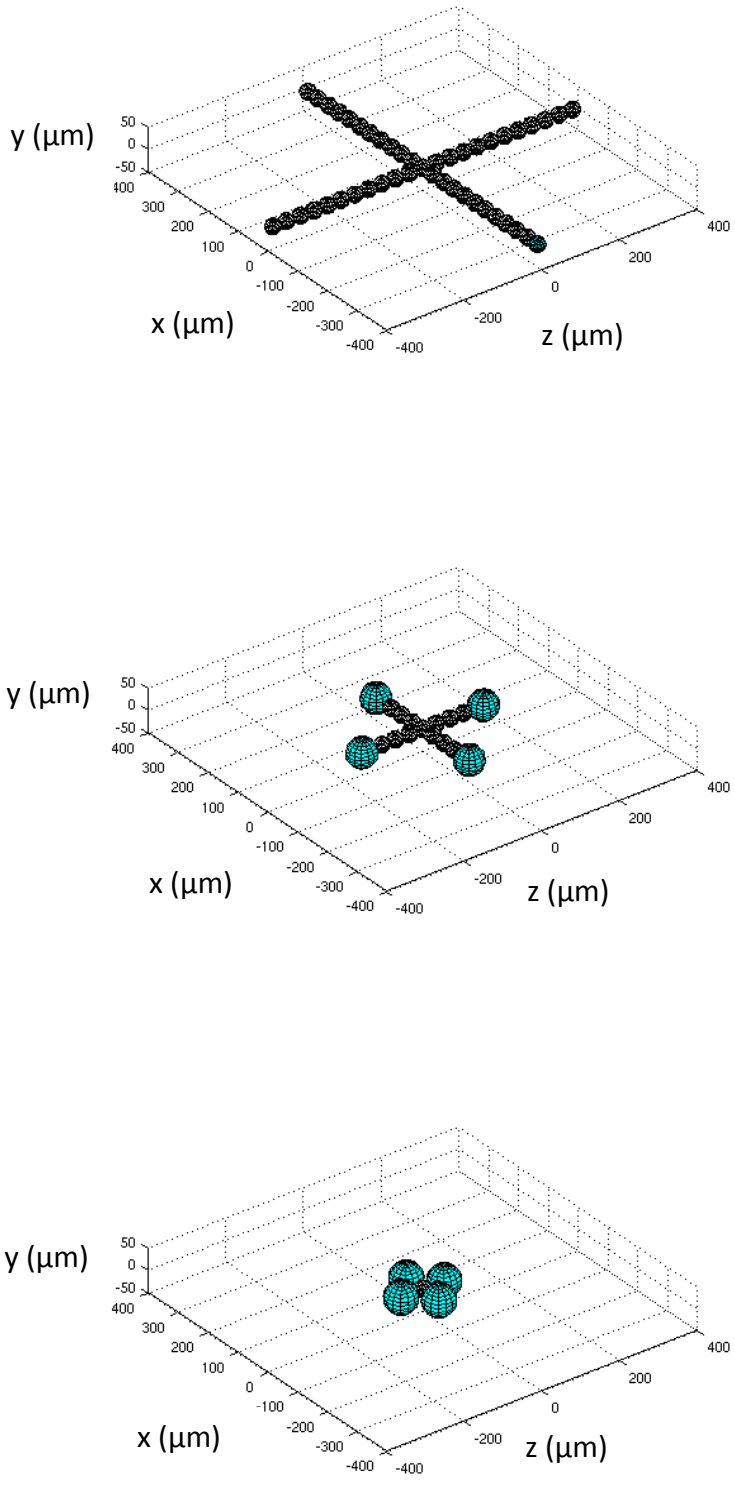

Figure 4. Diagram of the process of melting a cross crystal (L=750 μm).

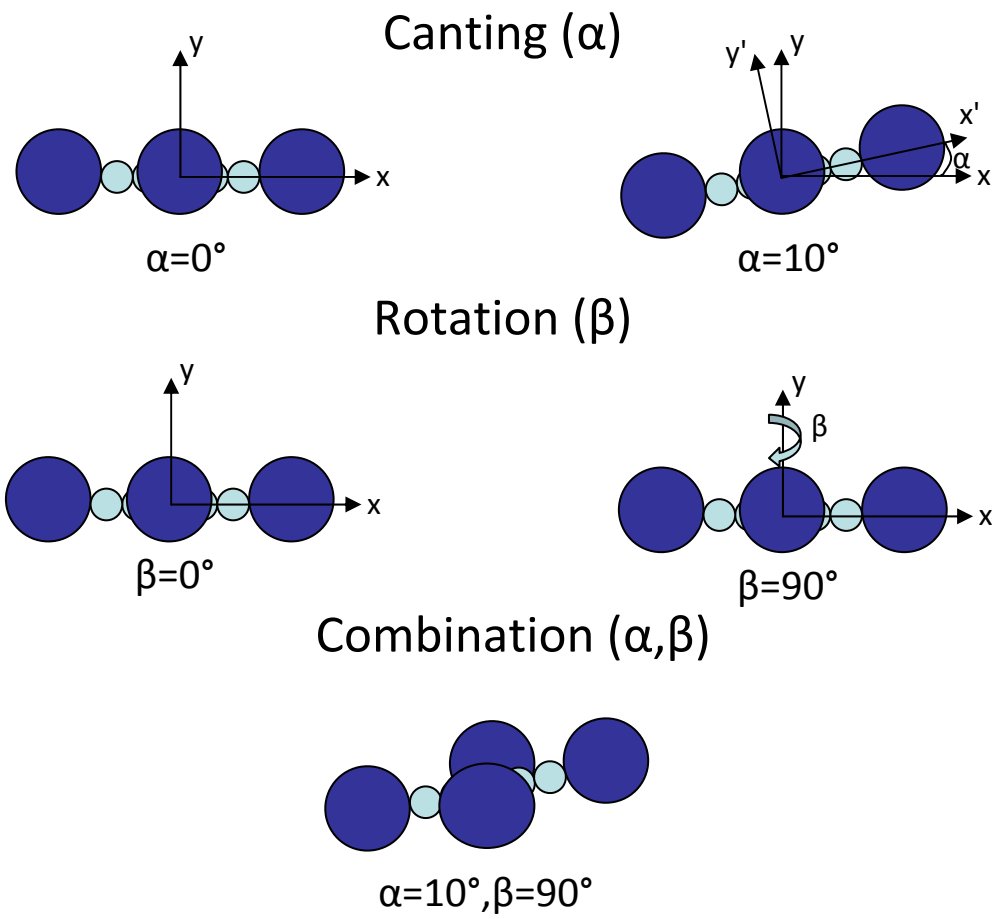

Figure 5. Illustration of rotation and canting of a cross crystal multi-sphere configuration. In this case, the *z*-axis points from the reader into the paper.

Chapter 4

Results

Results are shown below for the interaction of two spheres of varying size, columnar crystals of varying size, and cross-shaped crystals of varying size.

Two Sphere Solutions

The differential reflectivity (Z_{DR}) of two spheres located along the *x*-axis is shown in Figure 6 below. As expected, Z_{DR} is greatest for the case of two water spheres, with a lower Z_{DR} value for the case of a water and an ice sphere; two ice spheres produced the lowest Z_{DR} value. This effect is greatest when the spheres are nearly touching; the two water droplets produced a Z_{DR} almost 1.5 dB higher than the water and ice spheres. In all cases, the Z_{DR} rises sharply as the spheres become close, especially for the case of two water spheres. Interestingly, the plots for the different size spheres become superimposed when Z_{DR} is plotted against the ratio of the distance between spheres to the radius of the spheres. The effect of the radar wavelength is shown in Figure 7. Z_{DR} decreases slightly as the wavelength decreases; the trend shown in Figure 7 applies to the spheres of 20 μm, 50 μm, and 100 μm radius as well.

The two sphere exercise clearly shows that the spheres' interaction does not impact Z_{DR} until the distance between the drops approaches approximately 6 times the drop radius. V02 is correct in stating that the water droplets can produce anomalous scattering as they approach one another. While the water-water interaction is stronger than ice-water and ice-ice interactions, the latter two are significant, supporting the Baker and Verlinde (2004) conclusion that the ice structure cannot be ignored, especially considering that the ice is in constant, direct contact with the water droplets during melting.

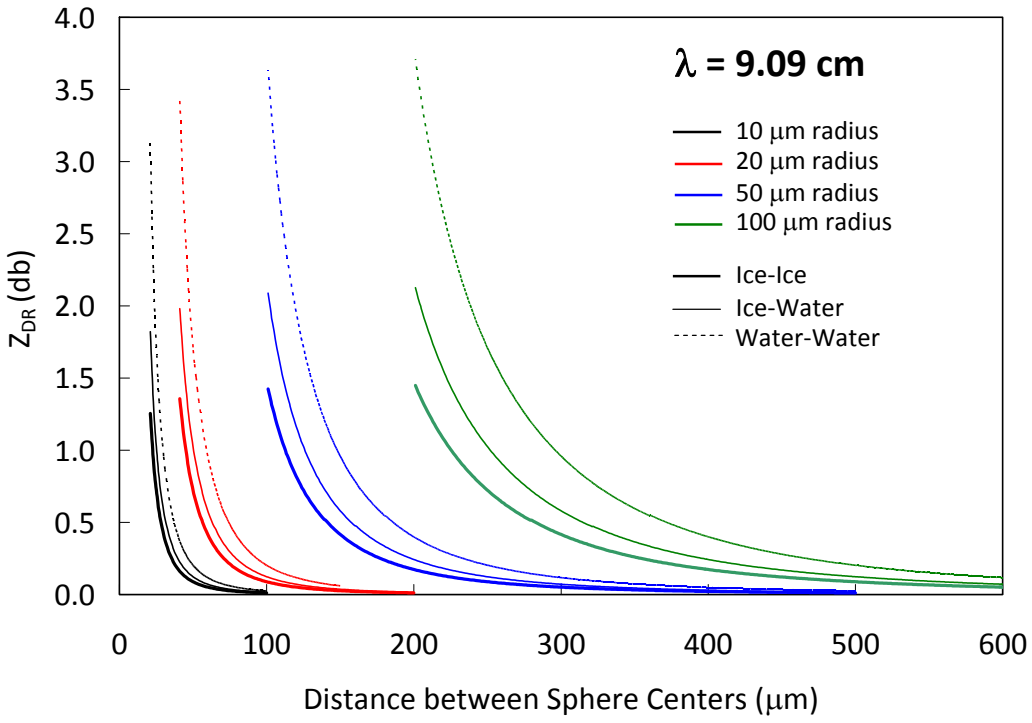

Figure 6. Z_{DR} of two spheres as a function of the distance between sphere centers.

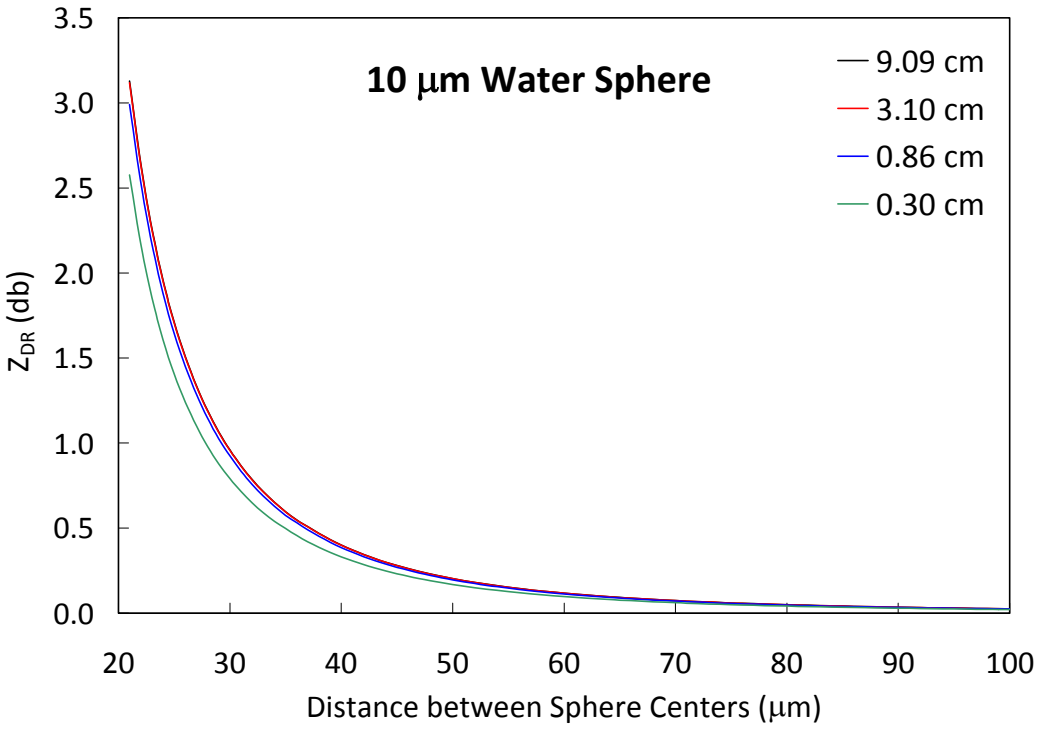

Figure 7. Z_{DR} at several different radar wavelengths of two 10 μm water spheres.

Column Solutions

Columns of ice spheres were melted according to Figure 3 while calculating the resulting Z_{DR} at each melt step. In the simplest case, a column is melted while remaining horizontal to the ground and perpendicular to the incoming radar beam. Figure 8 shows the results for all sizes at 0.86 cm wavelength and for all wavelengths for a crystal 3000 µm in length.

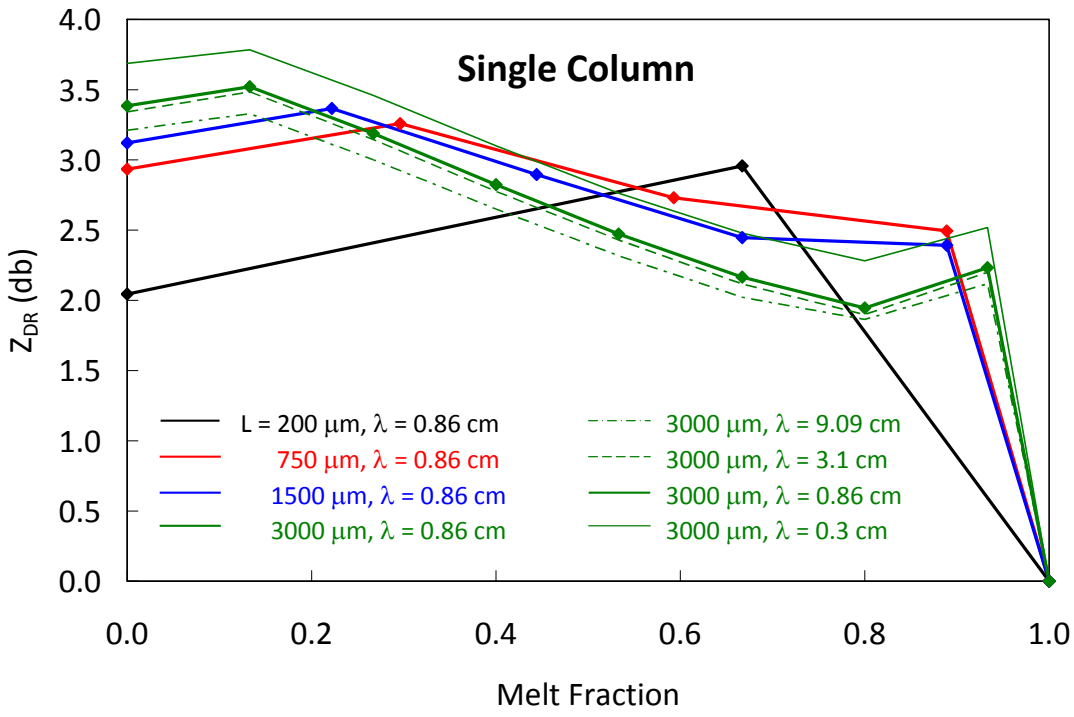

Figure 8. Z_{DR} for a single column crystal for all sizes.

The initial melt fraction of 0.0 corresponds to a hydrometeor completely comprised of ice. The initial Z_{DR} values for the 200 µm column are higher than the results for all of the two ice sphere cases, illustrating the strong shape effect on Z_{DR} even for an ice-only hydrometeor. In another example, a column 3000 µm in length is composed of spheres that have an approximate radius of 100 µm (see Table 1). Figure 6 tells us that two spheres with a radius of 100 µm with 200 µm separation between sphere centers would have a Z_{DR} of approximately 1.5 dB for λ = 9.09 cm. Figure 6

shows us that the Z_{DR} of the initial ice-only 3000 μm column is closer to 3.4. The increased Z_{DR} for these initial columns is expected considering the definition of Z_{DR} and its relation to the aspect ratio of the object.

Once melting begins, the two outermost ice spheres change into liquid water. Based on the results of the two sphere study, we expect to see the water spheres interact with each other to noticeably impact Z_{DR} when the distance between their centers is less than 6 times their radius. Table 2 shows us that the initial water spheres will interact with each other to impact Z_{DR} only for the column 200 μm in length. This explains why, in Figure 8, we see an initial increase in Z_{DR} during the initial melt step of approximately 50% for the 200 μm column while we see less than 10% increase in Z_{DR} for the larger size columns.

Table 2. Prediction of interaction of initial melt drops for column crystals based on distance between melt drops.

Approx. crystal length (*L*, μm)	Column thickness (*d*, μm)	Number of initial spheres	Approx. initial distance between outer spheres (μm)	Approx. six times radius of initial water spheres (μm)	Initial melt drops interact?	~ % increase in ZDR for initial melt step
200	63.8	3	130	190	Yes	50%
750	113.7	7	680	340	No	9%
1500	153.9	9	1230	460	No	6%
3000	208.4	15	2910	620	No	3%

As melting of the simple column continues, the Z_{DR} steadily decreases, a result of the reduction in length of the column (the shape effect). At the final step before complete melting, we see a change in the rate of decrease of Z_{DR} and even an increase in the magnitude of Z_{DR} for the 3000 μm column; it is at this point we can clearly see the effect of the two water droplets interacting to increase Z_{DR}. At the final step, only one ice sphere, with a diameter equal to the original thickness of the column, separates the two water spheres. Although the shape of the melting hydrometeor appears to dominate the Z_{DR} trend during most of the melting for the case of this single column, the impact of the two water spheres interacting is dominant when they are very close.

While the simple single column model for melting was able to show some slight increases in Z_{DR} during melting, the simulation did not produce the typical Z_{DR} maxima and variation found in field data from polarimetric radar. Developing the column model further, we introduced canting and rotation of the hydrometeors over 500 realizations as discussed in Chapter 3. The average results from the simulations (Figure 9) are very consistent with the trend displayed in Figure 8; however, the average Z_{DR} values are approximately 1.0-1.5 dB less than the case for the single column crystal. The reduction can be explained by the introduction of rotation of the hydrometeors into the model, which acts to reduce the horizontal projection of the hydrometeor encountered by the incident beam (see Figure 2). Of great interest is the variance of the data displayed in Figure 7.

Figures 9 and 10 depict the Z_{DR} and variance at λ = 9.09 cm and 0.3 cm, respectively, for all size crystals. The variance of the data is quite consistent for all cases except the 3000 μm column. The large spike in variance for the 3000 μm column is worth noting and may support V02's premise and shows a source for the higher Z_{DR} variance numbers seen in the radar bright band.

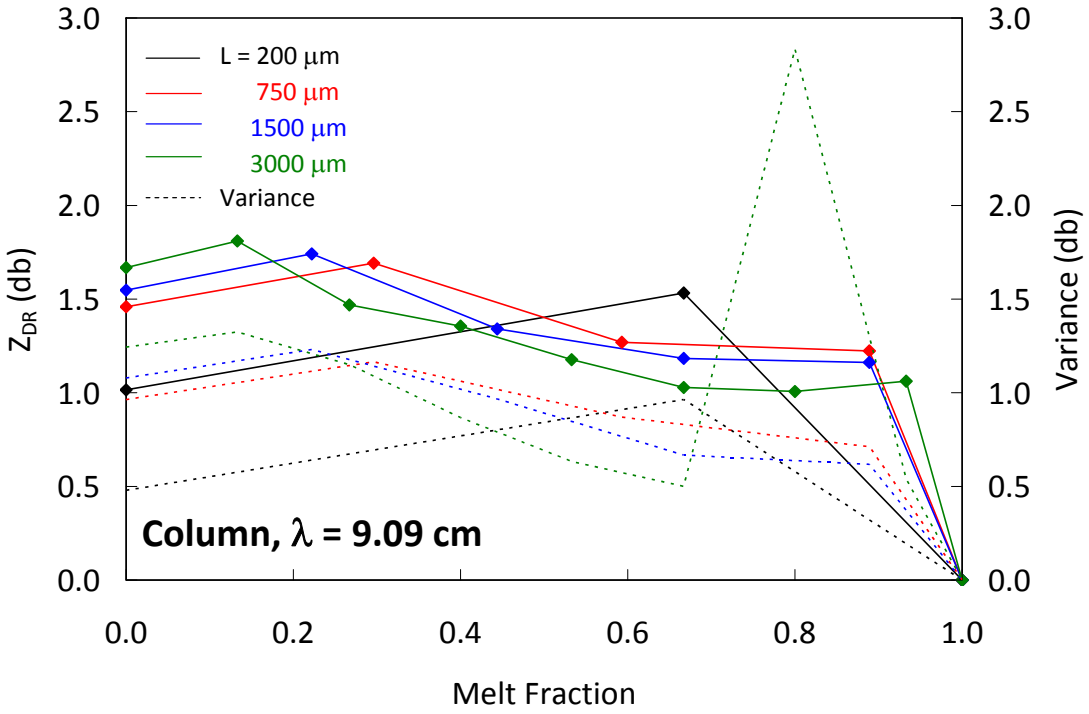

Figure 9. Z_{DR} and variance at λ = 9.09 cm for melting columnar crystals.

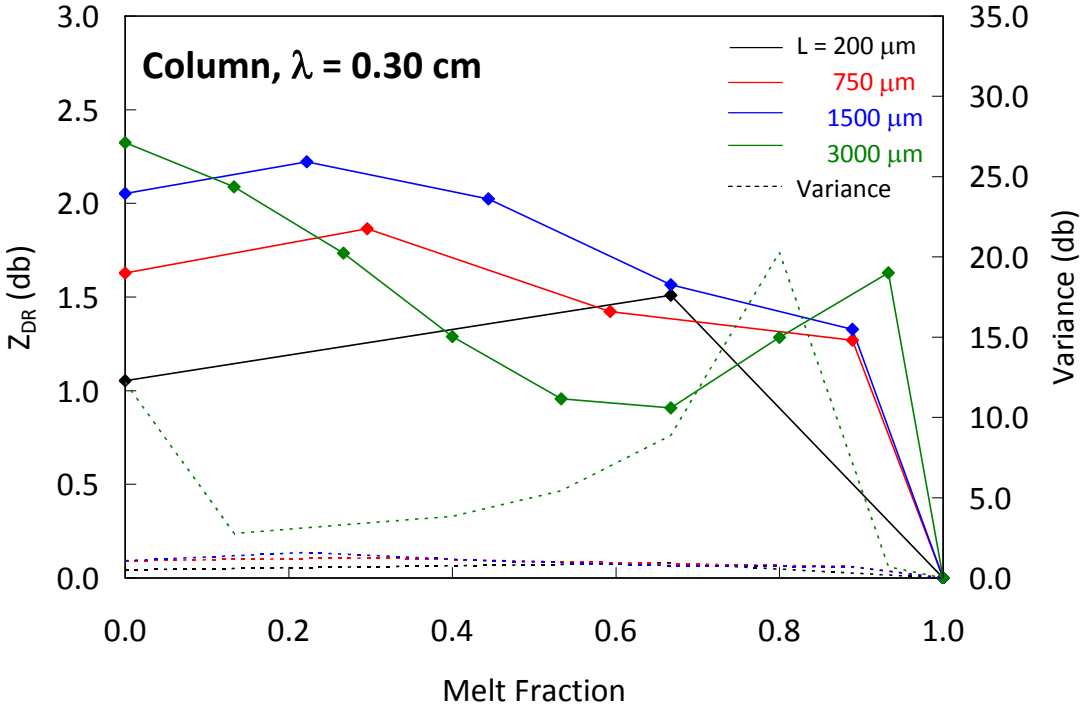

Figure 10. Z_{DR} and variance at λ = 0.30 cm for melting columnar crystals.

The magnitude of the variance, larger than the value of Z_{DR} for the simple column, might at first glance appear surprising considering the value of Z_{DR} for the simple column lying along the x-axis produces the highest possible Z_{DR} value. The large spike can be explained by the introduction of canting and rotation of the crystals. The geometry of the rotation and canting is illustrated in Figure 2. Note that throughout the text, we use the term horizontal to refer to the *x*-axis and vertical when referring to the *y*-axis. Canting will act to reduce Z_{DR} by shortening the horizontal component (*x*-axis projection) and increasing the vertical component (*y*-axis projection) encountered by the incident radar signal. Considering that the magnitude of the canting angle (α) changes by only ± 10°, we do not expect to see a significant effect on Z_{DR} from this source alone; however, including the rotation (β) of the crystals up to 90° provides an enormous source of variance. Imagine the extreme case where the user manipulates α to 10° and β to 90°. The resulting scattering properties of this crystal would be dominated by a larger vertical projection, producing a negative Z_{DR}. The presence of negative Z_{DR} values leads to enhanced Z_{DR} variance. The excessive spike in variance in Figure 10 for the case of the 3000 μm column at λ = 0.30 cm and a melt fraction of 0.8 is the culmination of water-water droplet interactions (V02) and the combination of rotation/canting effects producing negative Z_{DR}.

When comparing Figures 9 and 10, we see that there are differences in the Z_{DR} and Z_{DR} variance profiles that become more distinct for the largest columns. At a melt fraction of 0.8, the diameters of the two water spheres at the ends of the column are shown in Table 3 along with the total length of the column at that point. Figures 11 and 12 further examine the effect of radar wavelength. In contrast to the two sphere scenario, where the effect of λ is limited and produces only a small decrease in Z_{DR} with a decrease in λ, columns with a total length of 1500 μm and less experience a slight increase in Z_{DR} with decreasing λ. (Figure 11 is representative of both the 1500 μm and 200 μm cases.) For the case of the 3000 μm column (Figure 12), the results are more complex. Although the case for the $\lambda = 9.09$ cm is consistent with the results of the smaller columns, the 0.30 cm wavelength produced more extreme variations in the

average Z_{DR} with a severe spike in variance. Notice in Table 3 that the total length at a melt fraction of 0.8 is approximately 0.14 cm for the 3000 μm column. Enhanced variance is not totally surprising when considering that a maximum in backscatter from resonance scattering is predicted when the distance between two spheres is half of the wavelength. The reason that this effect produces only a small increase in average Z_{DR} while significantly impacting variance is that the column will be closest to ½ λ in its horizontal projection only when α and β are close to 0°. Still, the spike in variance for the 3000 μm column at λ = 0.30 cm is unexpectedly high. While we expect higher Z_{DR} fluctuations in this region, in an actual radar volume in nature, we would not see variation in Z_{DR} of this magnitude.

Table 3. Diameter of liquid water melt drops at the point of maximum variance, melt fraction 0.8.

Approximate crystal length (*L*) in μm	Original column thickness *d* (μm)	Diameter of water droplets at melt fraction 0.8 (cm)	Total length of column at melt fraction 0.8 (cm)
200	63.8	0.0066	0.032
750	113.7	0.016	0.066
1500	153.9	0.023	0.092
3000	208.4	0.037	0.14

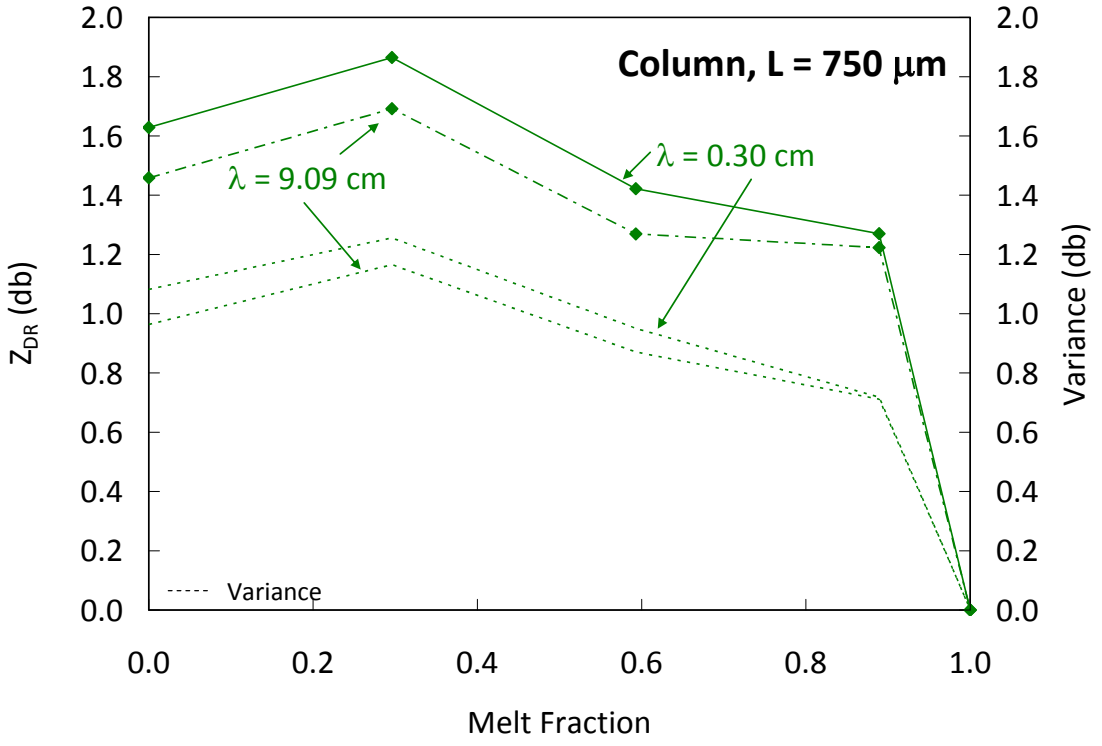

Figure 11. Z_{DR} and variance at λ = 0.30 and 9.09 cm for a column with L = 750 μm .

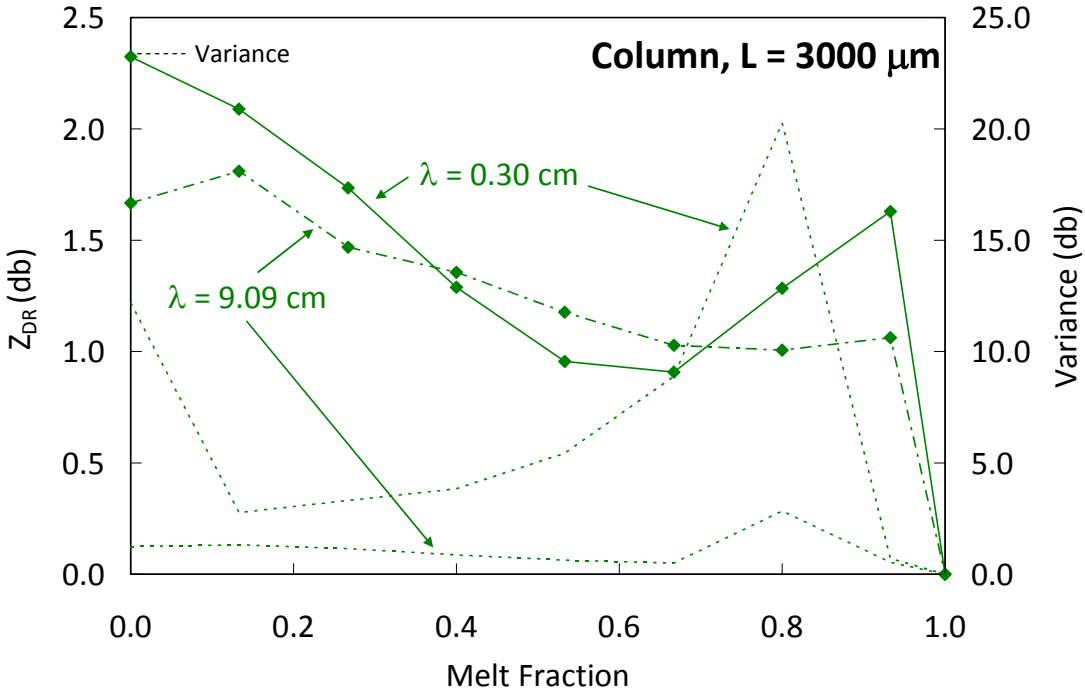

Figure 12. Z_{DR} and variance at λ = 0.30 and 9.09 cm for a column with L = 3000 μm.

The single column results, which use the refractive index, *N*, for actual water and ice at a particular wavelength, indicated that the shape of the hydrometeor plays an important role in the effect on Z_{DR} during much of the melting process. In order to investigate this effect further, the code was modified to isolate the effect of the shape of the hydrometeor on Z_{DR} from the effect of the presence of the water droplets, which possess a higher refractive index. In order to isolate the effect of the water-water interaction and its contribution to Z_{DR}, the code assigned all values of *N* for ice spheres to 1.0, in effect rendering them invisible while still allowing the simulation to maintain the spacing of the water droplets. Isolation of the shape effect is achieved by setting *N* for the water spheres to that of ice, producing an entire hydrometeor of ice throughout melting while keeping the size and shape of the actual mixed-phase hydrometeor. Figure 13 shows the results for the 750 µm column for a radar wavelength of 9.09 cm and is representative for the 3000 µm, 1500 µm, and 200 µm cases as well.

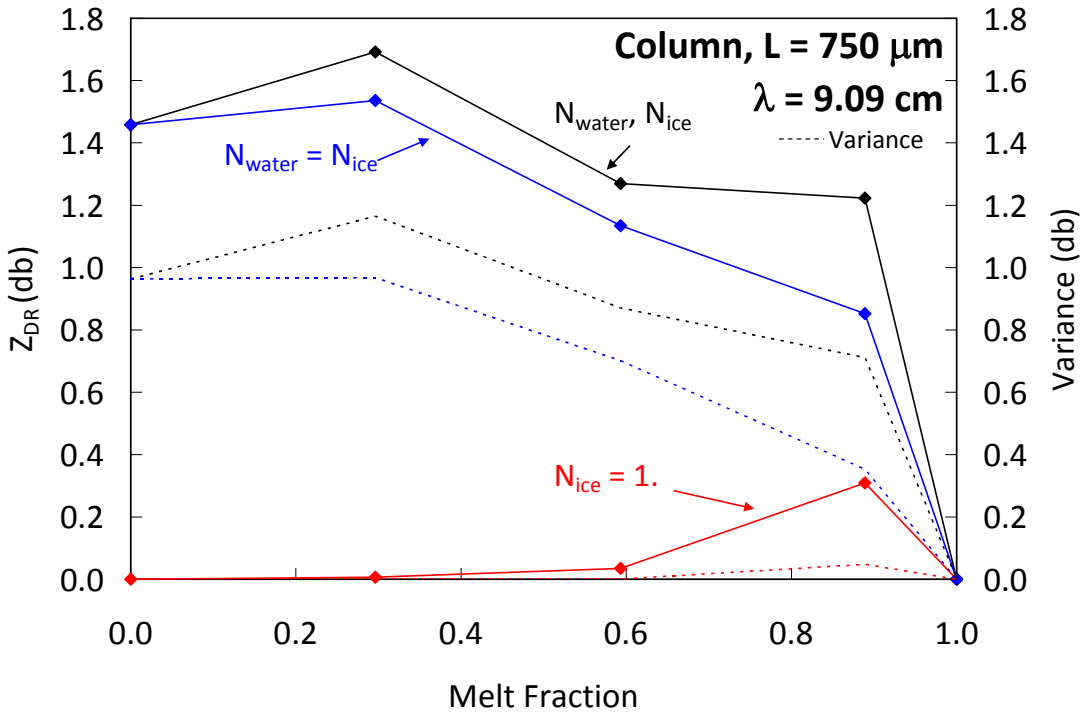

Figure 13. Z_{DR} and variance at λ = 9.09 cm for a 750 µm column showing the impacts of shape and water-water interaction during melting.

During early stages of melting, the water-water interaction is negligible. This can be seen clearly in Figure 13 (red line) where the Z_{DR} representing the water-water interaction is zero until 50% melting is achieved. One can see that the separated water droplets do not interact at all early on and therefore the Z_{DR} remains zero, reflecting solely the shape of the individual droplets. This trend changes significantly at the last step before melting is completed when two larger water spheres are separated by a much smaller ice sphere. During this step the water spheres could be close enough for their individual electromagnetic fields to interact and therefore influence Z_{DR}, as opposed to the early melting stage when the shape effect dominates. This trend was very consistent over all wavelengths and sizes. Only for the 3000 μm column for λ = 0.30 cm did the results change noticeably (Figure 14).

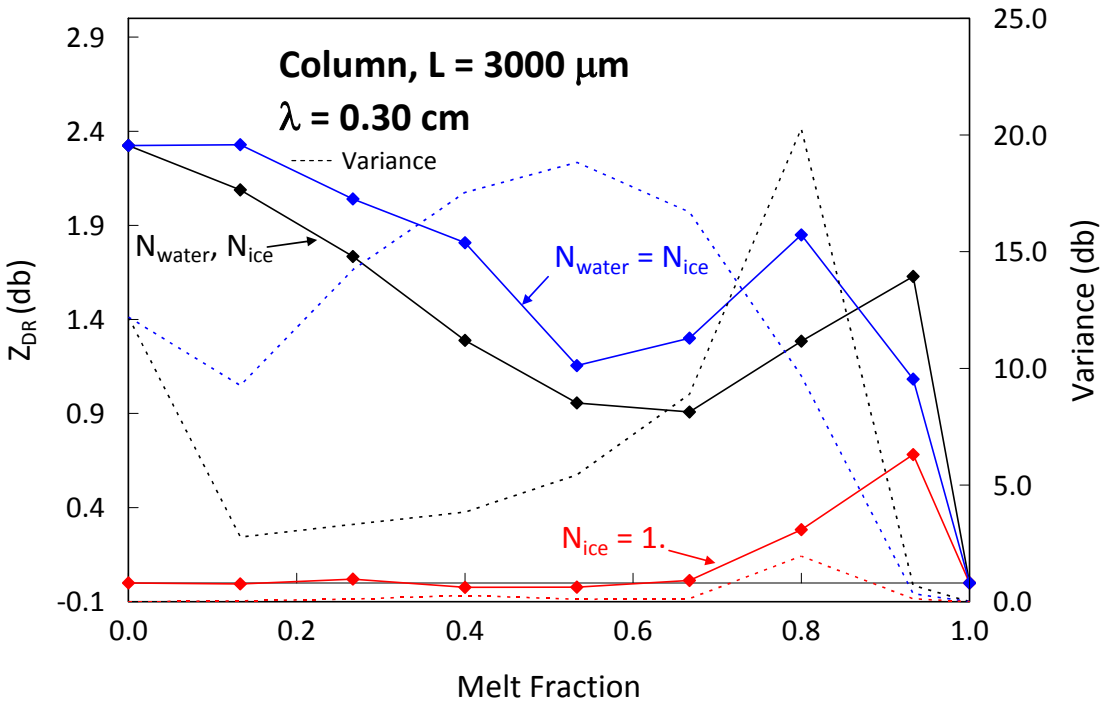

Figure 14. Z_{DR} and variance at λ = 0.30 cm for a 3000 μm column showing the impacts of shape and water-water interaction during melting.

The major change for this case was the increase in variance, which is expected based on previous results (Figures 10 and 12). The unexpected result is that the shape effect in this simulation actually exceeds the results for the true case where the refractive index of the water and ice are kept to their actual values. This reversal might be the result of the severe increase in variance due to resonance scattering; notice that the scale of the variance (the right *y*-axis in Figure 14) is much larger than in Figure 13.

Cross Solutions

Cross-shaped crystals comprised of ice spheres were melted according to Figure 4 while calculating the resulting Z_{DR} at each melt step. As presented in Figure 8 for the simple column crystal, Figure 15 displays the results of a single cross, oriented in the *x*-*z* plane with α and β equal to zero.

It is not surprising to see that both the initial Z_{DR} and the maximum Z_{DR} for each crystal size follow the same trend shown by the simple column crystal, with $Z_{DR,i}$ and $Z_{DR,max}$ increasing with increasing crystal size. Further comparison with the simple column crystal results, however, reveals some interesting and distinct differences. In the case of the column crystals, the maximum Z_{DR} was reached at the second to last step before melting when three ice spheres separate two larger water droplets. The simple cross crystal for λ = 0.86 cm experiences this maximum in Z_{DR} at the very last step before melting is complete. Additionally, the $Z_{DR,max}$ for cross crystals is much greater than $Z_{DR,max}$ for column crystals of approximately equal length due to the cross crystals' lesser relative sphere size, hence larger aspect ratio.

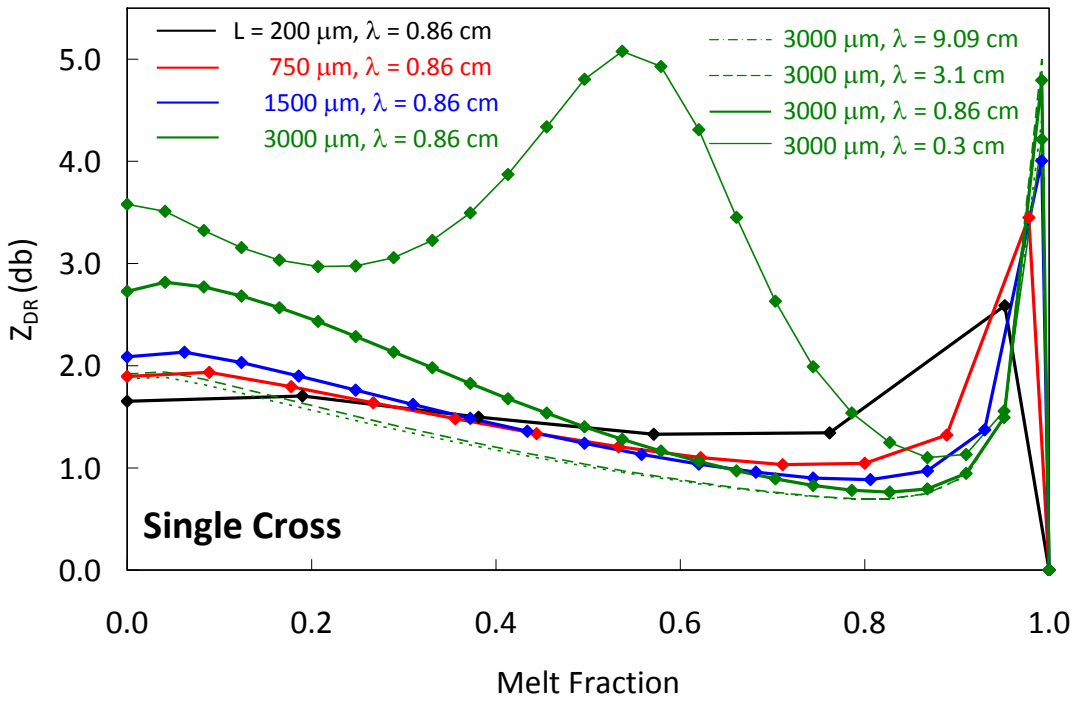

Figure 15. Z_{DR} for a single cross crystal.

In fact, this increased $Z_{DR,max}$ for the cross crystals results in a significant increase in Z_{DR} during the melting process and produces an overall Z_{DR} trend during melting that is much different for the cross crystals than for the column crystals. The large peak just before melting is completed for the cross crystals now becomes the most noticeable feature.

These significant differences between the simple column and cross crystals should be considered in light of the shape of the crystal encountered by the incoming radar signal for each case. The column crystal is initially uniform in shape and evolves to a much more distinct dumbbell shape as melting progresses (Figures 2 and 3). In the case of the cross crystals, the initial thin but long uniform linear shape is replaced by a dumbbell with a larger sphere in the center that corresponds with the size of the outer spheres (Figures 4 and 5). The difference in shape, although subtle early on in melting, does impact the overall Z_{DR} as the four larger spheres grow and eventually interact, supporting V02 and even showing the great impact this effect can have.

There are two additional notable traits for the case of the simple cross crystals. First is the prominent $Z_{DR,max}$ at λ = 0.3 cm for the 3000 μm cross at approximately 0.5 melt fraction. This localized maximum even exceeds the expected maximum in Z_{DR} just before melting is complete. At this point, the total length of the cross crystal is approximately 0.17 cm, very close to ½ λ for λ = 0.3 cm, and maximum backscattering is expected. The second noteworthy feature of the simple cross crystal solution can be seen when examining the effect of radar wavelength on Z_{DR} during melting. While the initial Z_{DR} values for the 3000 μm cross crystals follow the same trend for different λ as the simple column crystals ($Z_{DR,i}$ increasing with decreasing λ), the Z_{DR} peaks during the last step before melting do not follow a discernible trend and vary almost 1 dB across all λ (Table 4).

Table 4. Z_{DR} maximum at final step before melting completion for 3000 μm simple cross crystals.

λ (cm)	$Z_{DR, max}$	Melt fraction at $Z_{DR, max}$
9.09	4.4022	0.992
3.10	5.0011	0.992
0.86	4.7932	0.992
0.30	4.2163	0.992

Figures 16, 17, and 18 display the Z_{DR} results once canting and rotation are introduced over 500 realizations. Unlike the results from the column simulations, which have a more significant variance in Z_{DR} throughout the entire melting process, the cross crystals have negligible variance (on the order of 10^{-4} db) throughout the entire melting process until the last step before melting is completed. The consistent Z_{DR} results during the early stages of melting for the cross as compared to the column can be explained partially by the effect that the perpendicular arms would have in reducing the variation of the shape encountered by the incident beam as a result of the random assignment of β (see Figure 5).

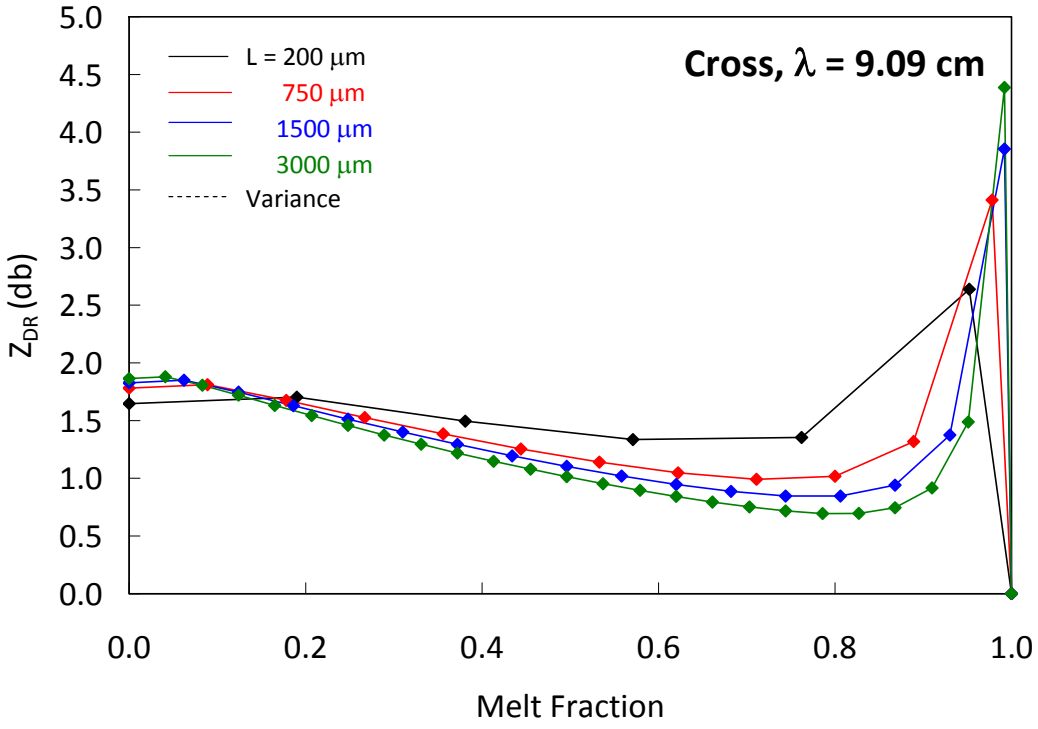

Figure 16. Z_{DR} at λ = 9.09 cm for cross crystals of varying size.

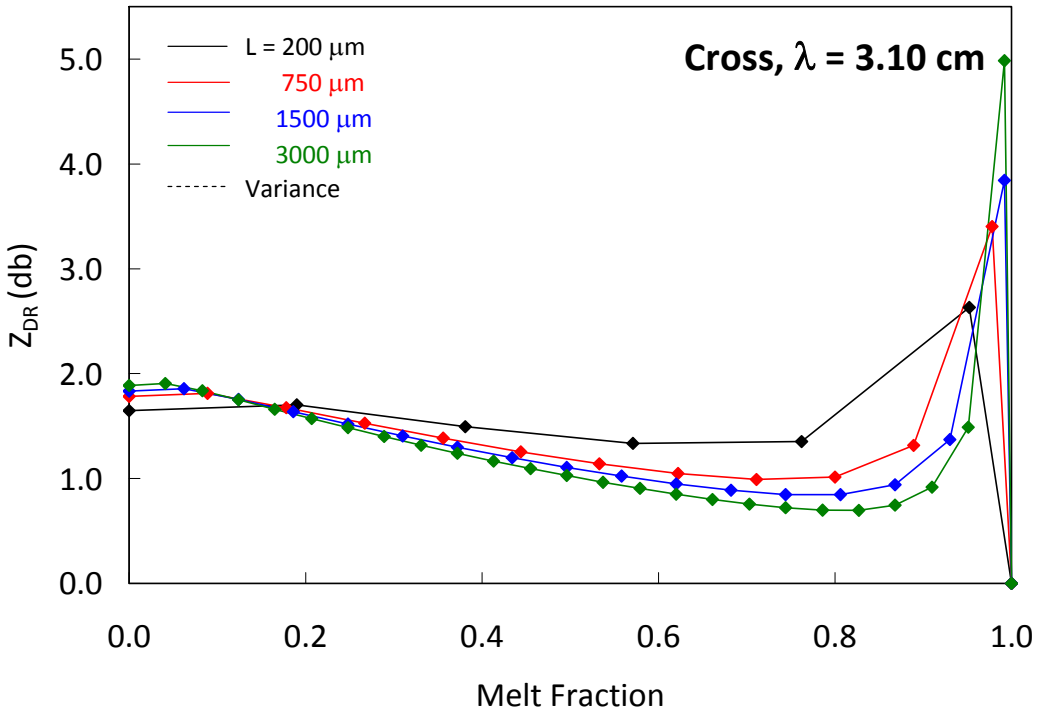

Figure 17. Z_{DR} at λ = 3.10 cm for cross crystals of varying size.

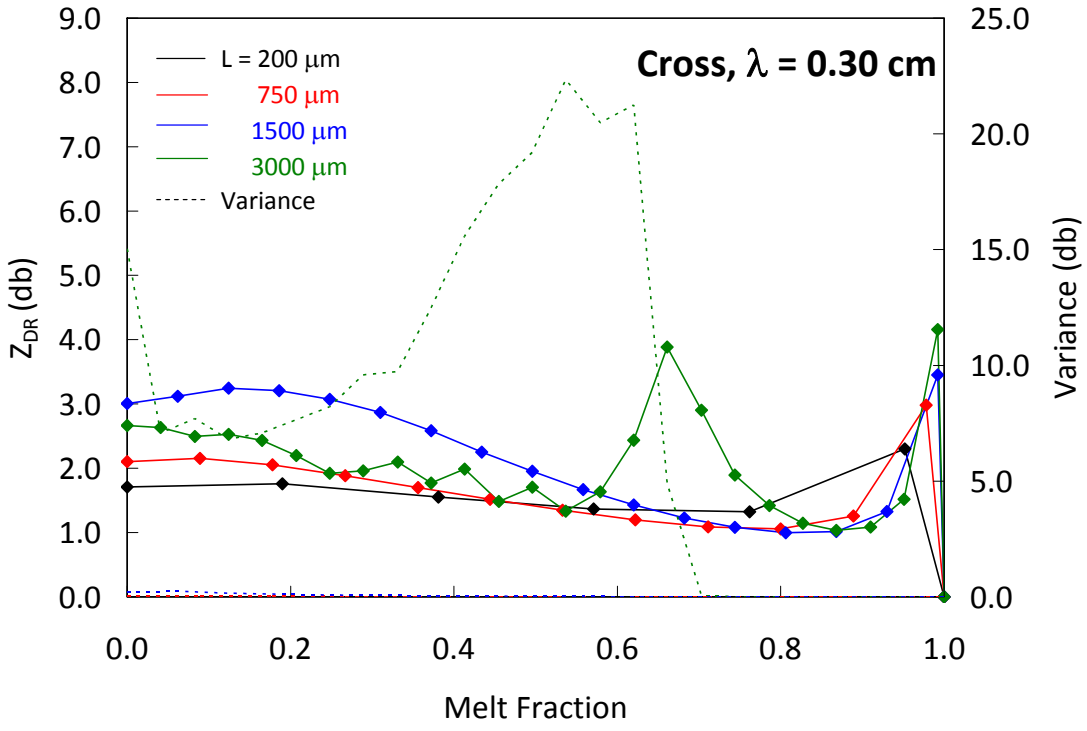

Figure 18. Z_{DR} at λ = 0.30 cm for cross crystals of varying size.

The negligible variance for the cross crystals applies to all cases except for the 3000 μm crystal at λ = 0.3 cm (Figure 18). Notice the oscillatory Z_{DR} results at λ = 0.3 cm for the 3000 μm cross crystal with a corresponding spike in variance for melt fraction 0.3 through 0.7. When we look at the results for all wavelengths for the 3000 μm cross crystals in Figure 19, it is clear that resonance scattering is only seen at the shortest wavelength (0.3 cm) when the total length of the crystal is close to ½ λ. Notice that the peak in variance is at a melt fraction of 0.5, corresponding to the peak in enhanced backscattering that is evident in Figure 15 for the simple cross.

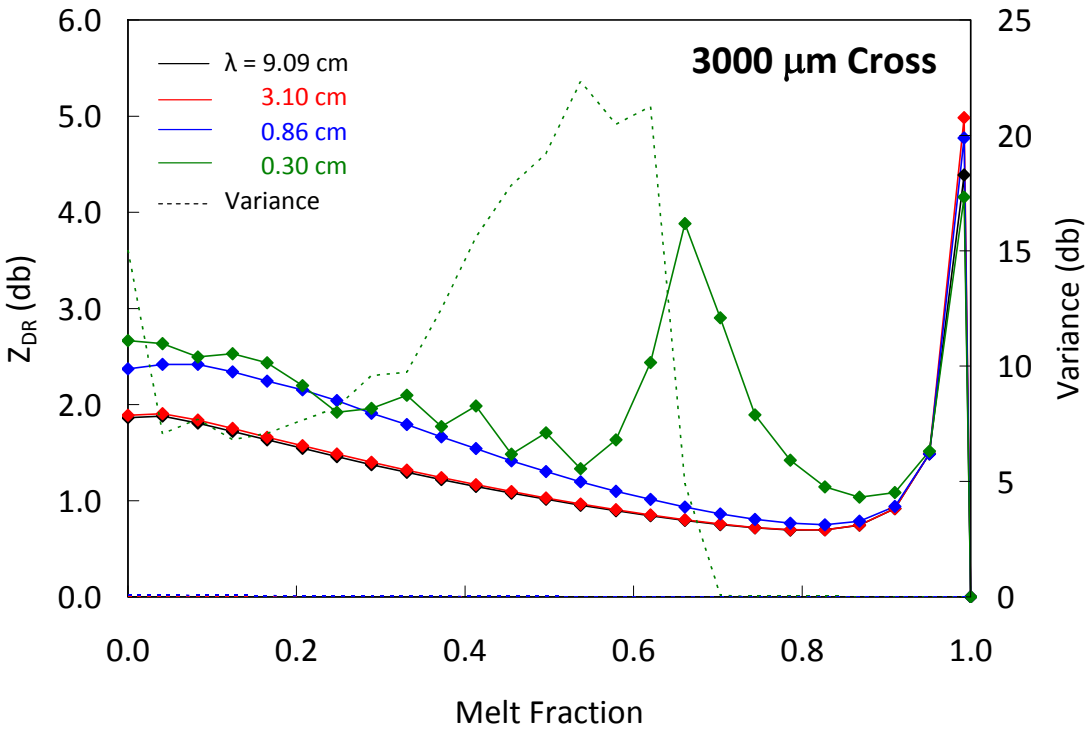

Figure 19. Z_{DR} over varying λ for 3000 µm cross crystals.

The results shown in Figures 20 and 21 examine the water droplet interaction and shape effects during melting, as discussed for the column crystals in Figures 13 and 14. The water droplet interaction effect for the cross crystals does not impact Z_{DR} until the very last steps in melting, as in the case for the column solutions. Unlike the columns, where the total Z_{DR} during the step before melting has a larger contribution from shape than water droplet interaction effects, the impact from these effects is more complex and extreme.

The 200 µm cross (Figure 20) displays fairly predictable results, with shape effects dominating during most of the melting process and water droplet interaction rising sharply during the step prior to completion of melting.

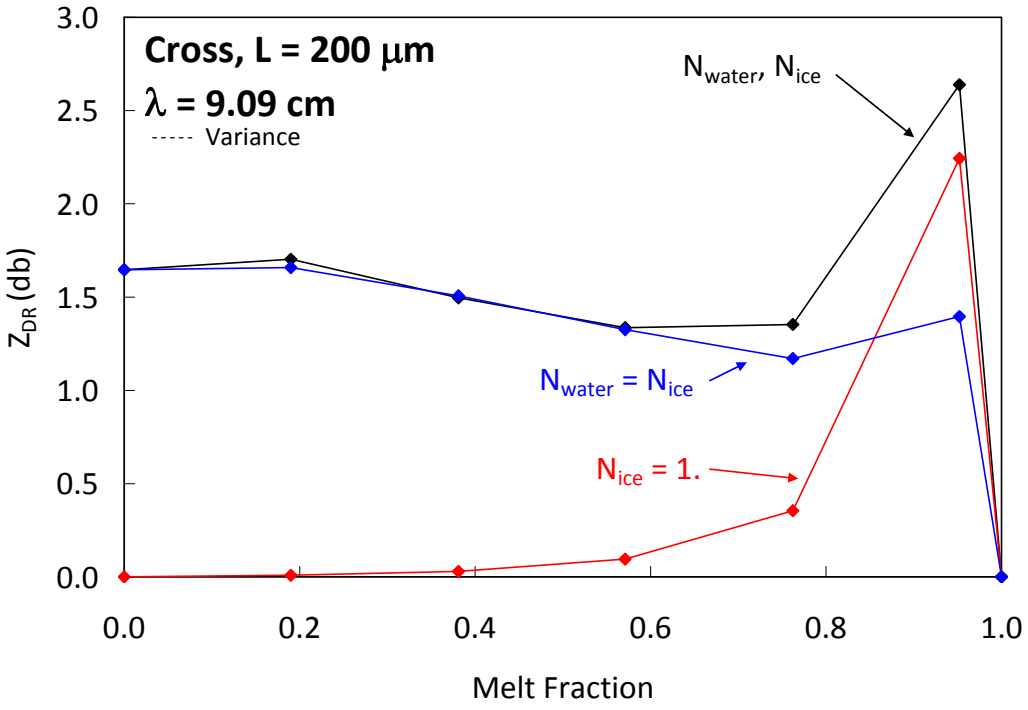

Figure 20. Z_{DR} at λ = 9.09 cm for a 200 μm cross showing the impacts of shape and water droplet interaction during melting.

Once the size of the cross is increased to 750 μm, the results become more unexpected, with the shape effect independently exceeding the actual Z_{DR} at a certain period during melting (Figure 21). We also find that the water droplet interaction effect is stronger relative to the 200 μm cross crystals; this is not unexpected given that the size of the water droplets just before melting will be larger for the larger crystals. We found that the results for the 750 μm cross crystal were consistent with 1500 and 3000 μm cross crystals for all wavelengths.

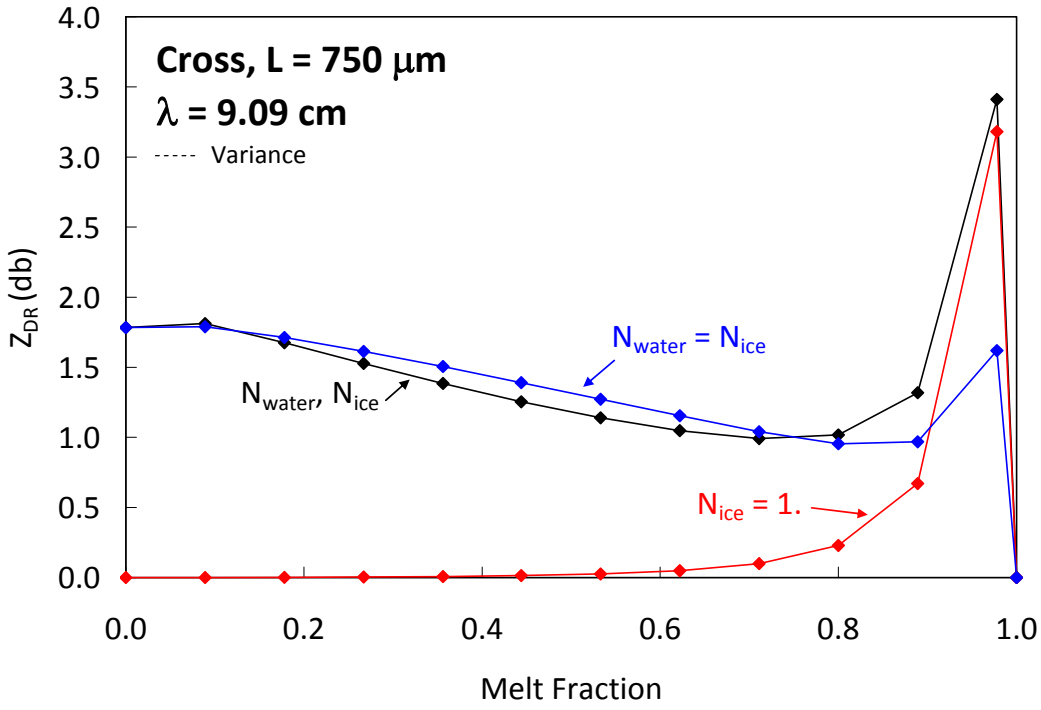

Figure 21. Z_{DR} at λ = 9.09 cm for a 750 μm cross showing the impacts of shape and water droplet interaction during melting.

Chapter 5

Discussion and Conclusions

In general, the simplified approach to modeling column and cross-shaped crystals using Mackowski's cluster of spheres computational model for determining the polarimetric scattering properties was able to replicate phenomenon of a sudden increase and wide variation in Z_{DR} consistent with field data of the melting layer, known as the radar bright band. Although the bright band represents a complex physical process, the results presented here show that the effect of the water droplets migrating close together on a single crystal can have a significant effect on the Z_{DR} when they are in such close proximity that their respective electromagnetic fields induced by the incident radar beam interact.

The rudimentary two sphere solutions supported V02's premise and provided understanding for interpreting the column and cross solutions. The column crystal simulations show that the column geometry contributes to a slight positive Z_{DR} during the entire melting process, but does not contribute to the extreme maxima in Z_{DR} as noted in field observation. The columns also produce a significant variance in Z_{DR} throughout the entire melting process. According to the results of the simulations, the cross crystals are similar to the columns early in melting by contributing to the slight positive Z_{DR}. However, they do not have any significant variance in Z_{DR} during melting until the last step before melting is complete when the Z_{DR} of the cross crystals rises sharply and produces a significant maximum consistent with the high Z_{DR} levels seen in the bright band.

The manipulation of the refractive index to isolate the shape and water droplet interaction effects produced interesting results. The results for both the column and cross solutions show that shape effects dominate during all of melting except for the last steps before melting is completed, when the water droplets at the ends of the crystal arms interact and contribute significantly to the Z_{DR}; the results are consistent for all sizes of columns explored. We also see that this model produces enhanced

backscatter at the shortest wavelength due to resonance scattering; this effect is most notable for the largest cross crystals.

The most logical progression of the simulation is to develop more realistic aggregate shapes still using the multi-sphere scattering model. While extremely simplistic proxies were used in the present research, more sophisticated models should be developed to investigate the scattering from more realistic models. The use of spheres for modeling is flexible, yet simple, and can be developed to recreate much more complex hydrometeors.

References

Auer, Jr., H.A., and D.L. Veal, 1970: The dimension of ice crystals in natural clouds. *J. Atmos. Sci.*, **27**, 919-926.

Baker, K.M. and J. Verlinde, 2004: A new look at the bright band. 14th International Conference on Cloud Physics, Bologna, Italy.

Bohren, C.F., and D.R. Huffman, 1983: *Absorption and Scattering of Light by Small Particles*, Wiley.

Brown, P.R.A., and P.N. Francis, 1995: Improved measurements of the ice water content in cirrus using a total-water probe. *J. Atmos. Oceanic Technol.*, **12**, 410-414.

D'Amico, M., A. R. Holt, and C. Capsoni, 1998: An anisotropic model of the melting layer. *Radio Sci*., **33**, 535–552.

Draine, B.T., and P.J. Flatau, 1994: Discrete dipole-approximation for scattering calculations. *J. Opt. Soc. Am.*, **A11**, 1491-1499.

Drummond, F.J., R.R. Rogers and S.A. Cohn, 1996: A new look at the melting layer. *J. Atmos. Sci.*, **53**, 759-769.

Fabry, F. and W. Szyrmer, 1999: Modeling of the melting layer: Part II: Electromagnetic. JAS, **56**, 3593-3600.

Fabry, F., and I. Zawadzki, 1995: Long-term radar observations of the melting layer of precipitation and their interpretation. *J. Atmos. Sci.*, **52**, 838-851.

Klaassen, W., 1988: Radar observations and simulation of the melting layer of precipitation, *J. Atmos. Sci*., **45**, 3741–3753.

Mackowski, D.W, 1994: Calculation of total cross sections of multiple sphere-clusters. *J. Opt. Soc. Am.,* **11**, 2851-2861.

Meneghini, R., and L. Liao, 1996: Comparisons of cross sections for melting hydrometeors as derived from dielectric mixing formulas and a numerical method, *J. of Appl. Met*., **35**, 1658-1670.

Mitra, S.K., O. Vohl, M. Ahr and H.R. Pruppacher, 1990: A wind tunnel and theoretical study of the melting behavior of atmospheric ice particles. Part IV: Experiment and theory for snow flakes. *J. Atmos. Sci.*, **47**, 584-591.

Pruppacher, H.R., and J.D. Klett, 1997: *Microphysics of Clouds and Precipitation*, Klewer Academic Publishers.

Russchenberg, H. W. J., and L. P. Ligthart, 1996: Backscattering by and propagation through the melting layer of precipitation: a new polarimetric model, *IEEE Trans. Geosci. Remote Sens*., **34**, 3–14. http://dx.doi.org/10.1109/36.481885.

Ryzhkov, A.V., and D.S. Zrnic, 1998: Discrimination between rain and snow with a polarimetric radar. *J. Applied Met..*, **37**, 1228-1240.

Seliga, T.A. and V.N. Bringi, 1976: Potential use of radar differential reflectivity measurements at orthogonal polarizations for measuring precipitation. *J. Applied Met.*, **15**, 69-76.

Skaropoulos, N. C., and H. W. J. Russchenberg, 2003: Simulations of Doppler spectra in the melting layer of precipitation. *Geophys. Res. Letters*, **30**, NO. 12, 1634, doi:10.1029/2003GL016959.

Straka, J.M., D.S. Zrnic and A.V. Ryzhkov, 2000: Bulk hydrometeor classification and quantification using polarimetric radar data: Synthesis of relations. *J. Applied Met.*, **39**, 1341-1372.

Szyrmer, W., and I. Zawadzki, 1999: Modeling of the melting layer. Part I: Dynamics and microphysics. *J. Atmos. Sci.*, **56**, 3573-3592.

Verlinde, J., D. Moisseev, Skaropoulos, N., W.F. v.d. Zwan, S.H. Heijnen and H.W.J. Russchenberg, 2002: Spectral Polarimetric Measurements in Mixed Phased Cloud. 11th Conference on Atmospheric Radiation, Odgen, Utah.

Xu, Y.-l., 1995: Electromagnetic scattering by an aggregate of spheres. *Appl Opt,* **34**, 4573–4588 (errata, *Appl Opt* 1998;37:6494, errata, *Appl Opt* 2001;40:5508).